Stoichiometry engineering of ternary oxide ultrathin films: BaxTi2O3 on Au(111)

Chen Wu, Martin R. Castell, J. Goniakowski, Claudine Noguera

Stoichiometry engineering of ternary oxide ultrathin films: $Ba_xTi_2O_3$ on Au(111)

Chen Wu,[1,2] Martin R. Castell,[1] J. Goniakowski,[3,4] and C. Noguera[3,4]
[1]*Department of Materials, University of Oxford, Parks Road, Oxford, OX1 3PH, United Kingdom*
[2]*School of Materials Science and Engineering, Zhejiang University, Hangzhou 310027, China*
[3]*CNRS, Institut des Nanosciences de Paris, UMR 7588, 4 place Jussieu, 75005 Paris, France*
[4]*UPMC Univ Paris 06, INSP, UMR 7588, 4 place Jussieu, 75252 Paris CEDEX, France*
(Received 23 December 2014; revised manuscript received 1 April 2015; published 21 April 2015)

Ternary oxide $Ba_xTi_2O_3$ ultrathin films on Au(111) substrates ($x \leqslant 2/3$) have been studied using a joint experimental and theoretical approach, including the use of scanning tunneling microscopy (STM), first principles calculations, and Monte Carlo simulations. The films are created by first covering the Au(111) substrate with a Ti_2O_3 (2×2) honeycomb (HC) network and then evaporating low concentrations of Ba atoms onto this film. STM imaging shows that the Ba atoms adsorb individually in the hollow sites of the HC network. Depending on the Ba coverage x, which ranges from 0 to 2/3, two ordered phases can be identified at $x = 1/3$ and $x = 2/3$. A disordered labyrinthlike phase is observed for values of x between 1/3 and 2/3. Theoretical modeling shows that the structural character of these films is driven by the charge transfer that occurs between the electropositive Ba atoms and the electronegative Ti_2O_3/Au substrate. This results in a number of calculated effects including an increase in the film rumpling and a reduction of the film work function with increasing x. The evolution of the structure of the thin films as a function of Ba coverage can be described by a lattice gas model with first-, second-, and third-neighbor Ba-Ba repulsive interactions. The range of the dipolar interactions is a key factor in understanding the behavior of Ba ordering. The structural and electronic flexibility, which can be engineered through stoichiometry, temperature, or support control, makes these ultrathin films promising materials for applications related to adsorption or reactivity, or as template supports for the growth of size-selected clusters.

DOI: 10.1103/PhysRevB.91.155424 PACS number(s): 68.37.Ef, 68.43.Bc, 68.43.De, 73.22.−f

I. INTRODUCTION

Spontaneous two-dimensional (2D) ordering of adspecies on surfaces has long been a subject of active research. These studies are motivated both by a development of an understanding of the fundamental nature of the adspecies-substrate interaction as well as a desire to create materials systems with novel properties that might lead to new applications. Over the years the focus has moved through very different systems, including alkali atoms on semiconductors [1], rare gas atoms on graphite [2–4], anions on metals [5], molecules on metals [6], etc. More recently, growth of ultrathin oxide films, usually on metallic supports, has been successfully performed, either with the aim of obtaining a patterned support for the formation of size-selected clusters for catalysis or magnetic recording purposes, or as an inverse catalyst system. When the film thickness is no more than one or two atomic layers, depending upon preparation conditions, these 2D films may display structures and stoichiometries that are not seen in bulk crystals as has been observed for example for the oxides of Al, Ti, V, Fe, Co, and Si [7–12].

Ordering of metal adspecies on ultrathin films may be driven by Moiré surface patterning due to the lattice mismatch [12–16] or by specific features, such as periodic holes [17]. Alternatively, repulsive adspecies-adspecies interactions may be involved, when charge transfer between the adspecies and the support takes place. It has been shown that the sign of the charge transfer is determined by the relative position of the adatom frontier orbitals with respect to the gap edges and/or the Fermi level of the supported film and that there is a coupling between the charge state of the adsorbate and the polaronic distortion of the film [18–22]. The importance of this charge transfer is reflected in the adatom-substrate and adatom-adatom interactions. This has a potentially significant effect on the adspecies morphology, with important consequences related to their catalytic properties. For this reason, transition and noble metal atoms have formed the focus of most studies [23–26], particularly within the context of single atom catalysis [27]. When adsorption of early transition metal or simple metal atoms is considered, a distinct situation arises. The charge state of the adsorbate is large and may be comparable with that of its corresponding oxide. These adsorbate systems, when ordered, should be considered as ternary 2D oxides with no equivalent in the bulk.

It is in this context that the present paper focuses on the model ternary system $Ba_xTi_2O_3$ obtained by the deposition of Ba adatoms on (2×2) Ti_2O_3 honeycomb ultrathin film grown epitaxially on a Au(111) substrate [12,28]. This system is to some degree related to $BaTiO_3$ ultrathin films, which are currently the subject of intense activity [29–33]. However our $Ba_xTi_2O_3$ system differs significantly due to its variable stoichiometry, and its distinct structure and electronic properties displayed for $x \leqslant 2/3$, which we have studied through scanning tunneling microscopy (STM), first principles modeling, and Monte Carlo (MC) simulations.

The paper is organized as follows. A description of the experimental and theoretical methods is given in Sec. II. The next part (Sec. III A) describes our STM results and *ab initio* modeling of isolated Ba adatoms on the bare Ti_2O_3/Au(111) substrate. We then calculate in Sec. III B the energetics of Ba-Ba interactions, followed by a section (III C) comparing STM images with MC simulations of Ba coverages up to the experimentally observed saturation limit of 2/3. The results of the calculations of the electronic structure of the $Ba_xTi_2O_3$ system are presented in Sec. III D. A discussion follows (Sec. IV) before the conclusion.

II. METHODS

The present study makes use of STM measurements, first principles calculations, and MC simulations. These are described individually in the following three sections.

A. Experimental methods

The experiments were carried out in a JEOL JSTM4500xt instrument, operating at UHV base pressure of 10^{-8} Pa. Mica-supported Au(111) single crystals (Agilent Technologies, UK) were used as the substrates. The Au(111) surfaces are first Ar^+ ion sputtered and then UHV annealed for 1.5 hours at 600 °C which results in the familiar herringbone reconstruction. Ti is deposited onto the reconstructed Au substrates from an electron beam evaporator (Oxford Applied Research EGN4) and the samples are then annealed at 600 °C in an O_2 atmosphere of 10^{-6} Pa. This gives rise to epitaxial (2×2) Ti_2O_3 honeycomb ultrathin films as described in detail in Ref. [12]. Ba deposition is then performed from a getter wire (SAES Getters S.p.A.) installed in a dedicated Ba evaporation system that is further described in Refs. [28] and [34]. The samples are then annealed in UHV at 600 °C for 40 minutes, so that ordered Ba structures are created. STM imaging is carried out at room temperature in constant current mode using electrochemically etched W tips with the bias voltage applied to the sample. The Ba coverage is calculated by examining the STM images and counting the number of Ba adatoms occupying the threefold hollow sites of the honeycomb Ti_2O_3 structure. Full Ba coverage [1 monolayer (ML)] is defined as full occupation of all the hollow sites of the honeycomb structure.

B. *Ab initio* computational details

The computational part of the study relies on a plane waves density functional approach, with gradient-corrected PW91 exchange-correlation functional [35], and the projector augmented wave method [36] implemented in VASP [37]. The Ti_2O_3/Au(111) support is represented by a slab composed of four atomic Au layers with a Ti_2O_3 layer adsorbed on one side only. Periodic slab images are separated by at least 11 Å of vacuum, and dipole corrections are used to eliminate the remaining spurious interactions. The experimental gold lattice parameter of 4.08 Å is systematically used in the calculations. Atomic positions of Ba adsorbates of all ions in the Ti_2O_3 film and of the Au surface atoms are fully optimized, while the remaining Au atoms are relaxed only in the direction normal to the surface (threshold on forces = 0.01 eV/Å). Fine calculations on structural and electronic characteristics of the 1/3 ML coverage are performed with a $(2\sqrt{3} \times 2\sqrt{3})R30^\circ$ surface unit cell and fine $(6 \times 6 \times 1)$ Monkhorst Pack sampling of the Brillouin zone. With these settings the Ba adsorption energy converges to within 0.01 eV/Ba. Simulations of model ordered configurations for a wide range of Ba coverages from 1/12 to 1 ML are performed to estimate the Ba-Ba effective interactions, and these are performed in a larger $(4\sqrt{3} \times 4\sqrt{3})R30^\circ$ surface unit cell with a $(1 \times 1 \times 1)$ Monkhorst Pack grid. Atomic charges are estimated according to Bader's prescription [38,39].

C. Monte Carlo simulations

The energetics of Ba adsorption and Ba-Ba interactions are mapped onto a lattice gas model of the form

$$E = \frac{1}{2} \sum_{i,j} J_{ij} n_i n_j. \quad (1)$$

The sites i represent the Ba adsorption sites, i.e., the hollow sites of the honeycomb structure. The sum of pair interactions is restricted to first, second, and third neighbors, with respective values J_1, J_2, and J_3. Occupation numbers n_i are either 0 or 1.

Standard importance sampling MC simulations are carried out at given parameter values $k_B T/J_1$, J_2/J_1, and J_3/J_2 and constant Ba concentrations on a two-dimensional hexagonal lattice of 36×36 sites with periodic boundary conditions. The Metropolis algorithm is applied to trial exchanges between filled and empty sites, with 500 000 Monte Carlo steps per site. Neglecting the first 10% of the steps in each run, the average numbers $\overline{N_1}$, $\overline{N_2}$, and $\overline{N_3}$ of first, second, and third neighbors around each occupied site are evaluated and snapshots of the final configurations are kept.

III. RESULTS

A. The Ti_2O_3 monolayer and adsorption of single Ba adatoms

Figure 1(a) shows an STM image of the clean (2×2) Ti_2O_3 lattice grown on Au(111) as described in Ref. [12]. Ti atoms appear bright in the STM image and form a honeycomb pattern where the O atoms sit on the bridge sites between

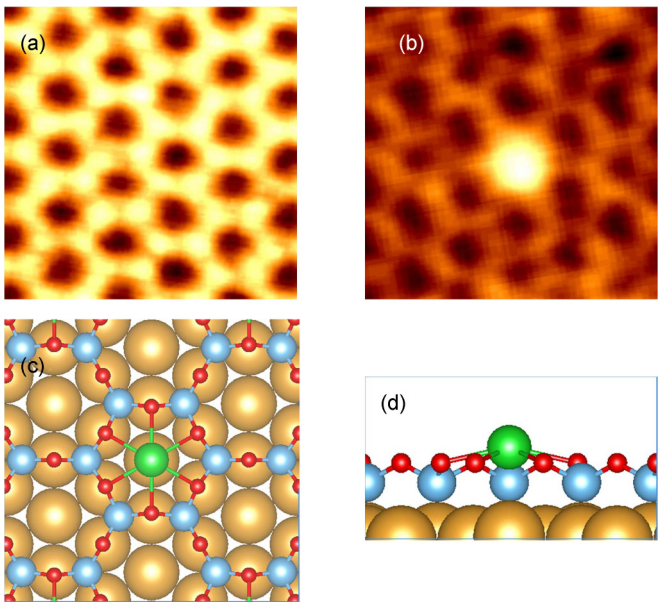

FIG. 1. (Color online) (a) STM image of the bare honeycomb Ti_2O_3 monolayer on Au(111) ($V_s = 0.98$ V, $I_t = 0.2$ nA, image size 2.9×2.9 nm^2). (b) STM image of a single Ba atom adsorbed on the honeycomb lattice ($V_s = 0.72$ V, $I_t = 0.2$ nA, image size 2.9×2.9 nm^2). (c) Top view ball and stick representation of a single Ba atom adsorbed on the Ti_2O_3/Au support, and (d) side view. Au, Ti, O, and Ba atoms are represented by yellow, blue, red, and green balls, respectively.

two neighboring Ti atoms. This structure is similar to the k-TiO_x/Pt(111) phase previously reported [40]. However, in the present case the Ti_2O_3 lattice is fully commensurate with a (2×2) Au(111) surface unit cell.

Additional information is provided by *ab initio* calculations for the experimentally determined registry of the Ti_2O_3 film with respect to the Au (111) surface. It is found that the Ti_2O_3 film develops significant rumpling $\delta z_{\text{Ti-O}} \sim 0.70$ Å, with the anions relaxing outwards and the cations approaching the Au(111) surface. This rumpling is much larger than in the unsupported film (0.28 Å) and likely arises from the in-plane compression of the oxide film, necessary for maintaining the preferential registry with Ti in hollow sites at the interface. Indeed the strong adsorption energy of the oxide layer on the gold surface (3.8 eV/Ti_2O_3) enforces pseudomorphism at the interface. This is associated with significant electron transfer towards the gold support (0.94 electrons per Ti_2O_3 unit) and an increase of the work function of the surface by about $\Delta W \sim 0.40$ eV. In the unsupported film, the cations bear a magnetic moment of about 0.7 μ_B, suggesting a formal Ti^{3+} oxidation state, consistent with the Ti_2O_3 stoichiometry. When the film is supported on the Au(111) substrate, these magnetic moments are entirely quenched, which is in line with the increased positive charge of the film.

Figure 1(b) is an STM image of a single Ba adatom occupying the hollow site of the honeycomb Ti_2O_3 structure. The Ba atom is not mobile on the surface over multiple STM scans indicating a strong chemical bond between the Ba and the hollow site. *Ab initio* calculations confirm that the Ba atom located in the hollow site of the honeycomb lattice is the energetically most favored atomic arrangement, with an associated adsorption energy of $E^0_{\text{ads}} = 6.22$ eV. Six Ba-O bonds are formed with the neighboring anions [Figs. 1(c) and (d)], with Ba-O bond lengths of 2.80 Å, close to those obtained for bulk BaO in the rock-salt structure (2.81 Å). Upon adsorption, the Ba adatoms become fully oxidized. From Bader analysis ~1.65 electrons are transferred towards the support, from which roughly one electron is accommodated by the oxide film, and the remaining electrons by the Au(111) substrate.

B. Energetics of Ba-Ba interactions from *ab initio* simulations

To determine effective Ba adatom-adatom interactions, a variety of model ordered configurations were simulated with various Ba concentrations and ordering. *Ab initio* modeling enabled us to calculate the energetics of the different Ba arrangements. Table I summarizes the Ba adsorption energies E_{ads} as a function of Ba coverage and also lists the changes in adsorption energy ΔE_{ads}, with reference to the lowest Ba coverage under consideration ($x = 1/12$ ML). Table I also gives the first N_1 (Ba-Ba distance 5.76 Å), second N_2 (Ba-Ba distance 9.98 Å), and third N_3 (Ba-Ba distance 11.52 Å) neighbor coordination numbers for the different configurations.

Assuming that the change of adsorption energy ΔE_{ads} (per Ba adatom) due to interaction between the adsorbates can be written as

$$\Delta E_{\text{ads}} = \tfrac{1}{2}[N_1 J_1 + N_2 J_2 + N_3 J_3],$$

TABLE I. Calculated energetic characteristics of $Ba_xTi_2O_3$/Au(111) model configurations as a function of Ba coverage. The column headings are Ba coverage x, absolute Ba adsorption energy E_{ads} (eV/Ba), change of Ba adsorption energy ΔE_{ads} (eV/Ba) with respect to that at 1/12 coverage, and number of first N_1, second N_2, and third N_3 Ba neighbors of each Ba adatom.

x	E_{ads} (eV/Ba)	ΔE_{ads} (eV/Ba)	N_1	N_2	N_3
1/12	6.22	0.00	0	0	0
1/6 A	5.99	−0.23	1	0	0
1/6 B	6.13	−0.09	0	2	0
1/6 C	6.14	−0.08	0	0	3
1/3	5.97	−0.25	0	6	0
1/2	5.56	−0.66	2	2	6
2/3	5.27	−0.95	3	6	3
1	4.91	−1.31	6	6	6

with $J_{1,2,3}$ the first-, second-, and third-neighbor effective Ba-Ba interactions, respectively, the data reported in Table I provide an estimate of $J_{1,2,3}$. Moreover, since at low coverage (1/6 ML) we have considered three different configurations (A, B, C) with Ba adatoms only in respectively first-, second-, and third-neighbor positions, we can extract separately the low coverage ($x = 1/6$) values of $J_{1,2,3} = 0.46$, 0.09, and 0.06 eV, and the high coverage ($1/2 \leqslant x \leqslant 1$) values of $J_{1,2,3} = 0.39$, 0.09, and 0.06 eV. We note that, while J_2 and J_3 vary very little with x, J_1 is noticeably reduced at higher coverage. The best fit across the range of configurations we have considered is achieved with $J_1 = 0.43$ eV, $J_2 = 0.09$ eV, and $J_3 = 0.06$ eV. This results in values of $J_2/J_1 = 0.21$ and $J_3/J_2 = 0.667$.

C. STM and MC structural determination of $Ba_xTi_2O_3$/Au

The structure of the $Ba_xTi_2O_3$ films on Au(111) was investigated through a combined STM and MC approach. Figure 2 shows a series of six STM images (upper panels) of the Ba adatom distributions for coverages ranging from low values of $x = 0.07$ up to close to the maximum observed coverage of $x = 0.62$. STM images for coverages exceeding $x = 2/3$ indicate that a completely different type of atomic ordering takes place where Ba no longer adsorbs on the Ti_2O_3 honeycomb hollow sites. For this reason our analysis is restricted to Ba coverages of $0 < x < 2/3$.

The lower panels in Fig. 2 show MC snapshots at the same coverages as indicated in the STM images. In order to obtain the best agreement between the experimental STM images and the MC snapshots, certain values of the MC parameters k_BT/J_1, J_2/J_1, and J_3/J_2 had to be selected. The calculations showed that reproducing the STM images over the full range of coverages implied strong constraints on the fitting parameters. The best agreement was obtained for $k_BT/J_1 = 0.1 - 0.2$, $J_3/J_2 \approx 0.666$, and $0.2 < J_2/J_1 < 0.25$. These results strikingly confirm the validity of the J_1, J_2, and J_3 values extracted from the independent *ab initio* calculations (see Sect. III B).

Taking into account the experimental value for the annealing temperature $T = 600\,^{\circ}$C, the snapshots shown in Fig. 2 were obtained for $k_BT/J_1 = 0.17$, $J_2/J_1 = 0.21$, and $J_3/J_2 = 0.666$, which are very close to the *ab initio*

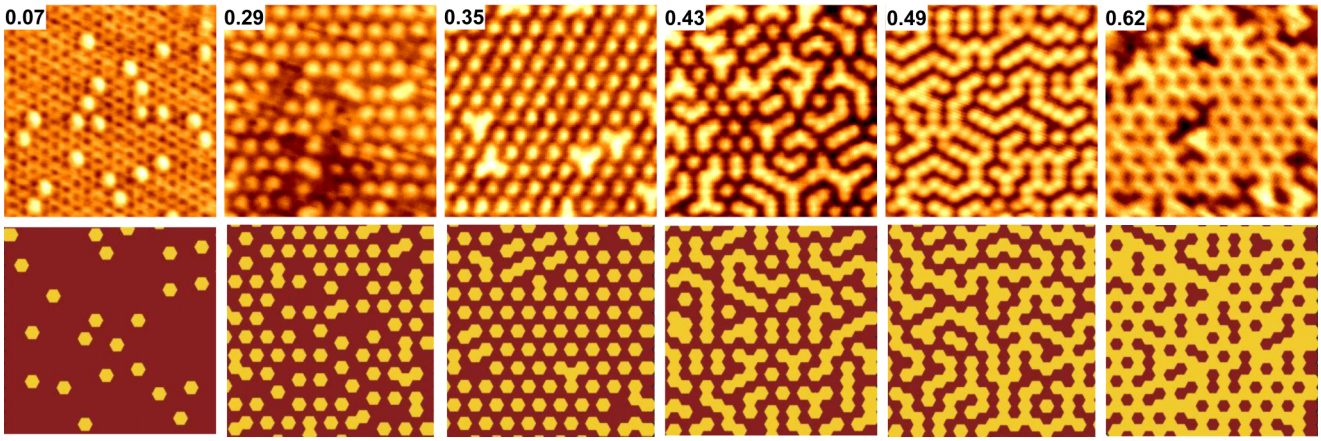

FIG. 2. (Color online) STM images (top panels) and Monte Carlo simulation snapshots obtained for $k_BT/J_1 = 0.17$, $J_3/J_2 = 0.666$, and $J_2/J_1 = 0.21$ (bottom panels). From left to right, the Ba coverage is $x = 0.07$, 0.29, 0.35, 0.43, 0.49, 0.62. Only the adsorption sites are represented, which are dark red when empty and yellow when occupied. Images sizes are 10×10 nm^2, and tunneling conditions for the STM images are V_s ranging from 0.35 to 1.00 V and I_t ranging from 0.18 to 0.28 nA.

predictions. As is clear from Fig. 2, the MC simulations account qualitatively well for the Ba atom distributions which are observed experimentally. At very low coverage ($x = 0.07$), randomly distributed Ba atoms are observed on the surface. With increased Ba deposition ($x = 0.29$), the configurations with first nearest neighbor (1nn) atoms are strongly suppressed, confirming 1nn repulsion, i.e., $J_1 > 0$. Aside from small thermal fluctuations, two ordered phases are found at $x = 1/3$ and 2/3, with the same $(2\sqrt{3} \times 2\sqrt{3})R30^\circ$ unit cell with respect to the gold surface. At $x = 1/3$, all second nearest neighbor (2nn) sites of a given Ba atom are occupied by another Ba atom, and all 1nn sites are empty. Empty and filled sites are interchanged in the $x = 1/3$ and $x = 2/3$ configurations. For coverages intermediate between 1/3 and 2/3 ($x = 0.35$, 0.43, and 0.49), the 1nn sites start to become occupied as well as the 2nn sites. This results in a disordered phase with a labyrinthlike pattern. Similar configurations have been found in other contexts, for example, in some 2D magnetic structures [41,42].

More quantitatively, Fig. 3 displays a comparison between the MC simulation results and an experimental measurement of the mean number of occupied 1nn and 2nn sites, $\overline{N_1}$ and $\overline{N_2}$, respectively, as a function of Ba coverage. $\overline{N_1}$ is close to zero up to $x = 1/3$ and then increases monotonically, while $\overline{N_2}$ presents two maxima at $x = 1/3$ and $x = 2/3$ and a minimum for $x \approx 1/2$. Such very good quantitative agreement between experiment and simulation shows that the theoretical analysis encompasses all the critical microscopic mechanisms that form the basis of the Ba-Ba interactions on the Ti_2O_3/Au(111) substrate.

D. Electronic structure of $Ba_xTi_2O_3$/Au from *ab initio* simulations

Table II summarizes the evolution of the main structural and electronic characteristics of the $Ba_xTi_2O_3$ ordered configurations ($x = 0$, 1/3 and 2/3), as determined from *ab initio* calculations. Regardless of the coverage, Ba adatoms transfer their electrons towards the support, giving rise to a positively charged $Ba_xTi_2O_3$ film. The Ba positive charge slightly decreases as x grows, tending towards values comparable with either bulk BaO (+1.45) or bulk $BaTiO_3$ (+1.52). The overall positive charge density of the films increases rapidly with x, and the negative charge density of the Au substrate increases proportionally.

The Ti_2O_3 film rumpling $\delta z_{\text{Ti-O}}$ also displays a strong variation as a function of x. Starting from a large positive value at $x = 0$, $\delta z_{\text{Ti-O}}$ increases in a quasilinear way with coverage, which correlates with the quasilinear increase of the *total* substrate charge density.

The combined effect of the interfacial charge transfer and of the Ti-O rumpling leads to large modifications ΔW of the

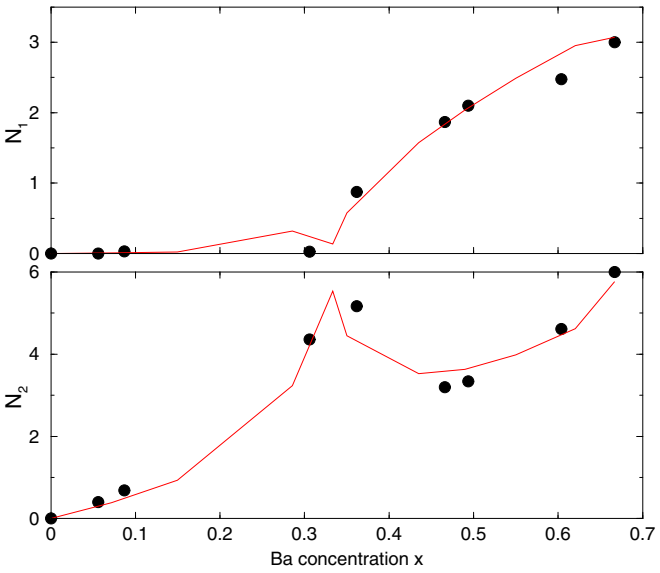

FIG. 3. (Color online) Variation of the mean number of first (top panel) and second (bottom panel) nearest neighbors as a function of Ba concentration x. Full lines are results of Monte Carlo simulations obtained for $k_BT/J_1 = 0.17$, $J_2/J_1 = 0.21$, and $J_3/J_2 = 0.666$. Black dots are experimental values extracted through STM image analysis.

TABLE II. Calculated structural and electronic characteristics of $Ba_xTi_2O_3$/Au(111) ordered phases as a function of Ba coverage x: charges Q_{Ba} of Ba atoms (e), total Au support charge density σ_{Au} ($e/Å^2$), elevation of Ba adatom with respect to the Au surface z_{Ba} (Å), Ti_2O_3 film rumpling $\delta z_{Ti\text{-}O}$ (Å), change of Au(111) work function ΔW (eV).

x	Q_{Ba} (e)	σ_{Au} ($10^{-3}e/Å^2$)	z_{Ba} (Å)	$\delta z_{Ti\text{-}O}$ (Å)	ΔW (eV)
0		−8.2		+0.70	+0.4
1/3	+1.61	−15.0	3.77	+0.79	−1.5
2/3	+1.55	−21.3	3.68	+0.86	−3.0

work function of the bare Au support. While positive at $x = 0$, ΔW becomes negative and its absolute value increases with x.

IV. DISCUSSION

We have shown that the ternary oxide ultrathin films consisting of $Ba_xTi_2O_3$/Au(111) display flexible structural and electronic characteristics which can be finely tuned through control of the Ba coverage x. The structural configurations are determined by the strength and range of the effective Ba-Ba repulsion induced by the oxidation of Ba upon deposition. From the $J_{1,2,3}$ values determined by *ab initio* calculations, as well as the values yielding the best agreement between MC simulations and STM images, the Ba-Ba interactions appear to be noticeably screened by the substrate. The $J_{1,2,3}$ values ($J_1 = 0.43$ eV, $J_2 = 0.09$ eV, and $J_3 = 0.06$ eV) scale roughly as the inverse third power of nearest neighbor site distances ($d_1 = 5.76$ Å, $d_2 = 9.98$ Å, $d_3 = 11.52$ Å), which is typical of dipole-dipole interactions, rather than as the inverse of atomic distances, which would be expected from unscreened Ba-Ba Coulomb repulsion. The strong electron transfer between the Ba adatoms and the support, which occurs upon adsorption, is responsible for this effect, since it results in a negative charge in the support, which counterbalances the positive charging of the Ba adsorbates.

While strong enough to stabilize the two ordered phases at $x = 1/3$ and $x = 2/3$, these interaction values do not succeed in overcoming the entropy term associated with thermal disorder in the labyrinth configurations when $1/3 \leqslant x \leqslant 2/3$ and in particular at $x = 1/2$. As shown in Fig. 4(b), by keeping the same J_2/J_1 and J_3/J_2 ratio values but lowering the temperature ($k_BT/J_1 = 0.02$ instead of 0.17), an ordered phase is found at $x = 1/2$ which consists of stripes in which each atom has two 1nn, four 2nn, and two 3nn. Small portions of such stripes may be recognized in the labyrinth patterns obtained when $1/3 < x < 2/3$ in Fig. 2. It is interesting to note that longer range interactions would also induce an ordered stripe phase at $x = 1/2$ [Fig. 4(c)], but with a periodicity different from the previous one, Fig. 4(b). The configuration shown in Fig. 4(c) was obtained with the same $k_BT/J_1 = 0.17$ value as the labyrinth phase, Fig. 4(a), but with effective unscreened Ba-Ba repulsions, decreasing as the inverse of distances ($J_2/J_1 = 0.57$ and $J_3/J_2 = 0.87$). In the ordered regions of this phase, each atom has three 1nn, two 2nn, and two 3nn. Due to the increased relative weight of 2nn and 3nn interactions, 1nn occupation is less inhibited and 3nn occupation more heavily penalized, compared to the stripe phase obtained with effective dipole-dipole interactions. This discussion highlights the structural flexibility present in this ultrathin film, which can be engineered through stoichiometry, temperature, or support control.

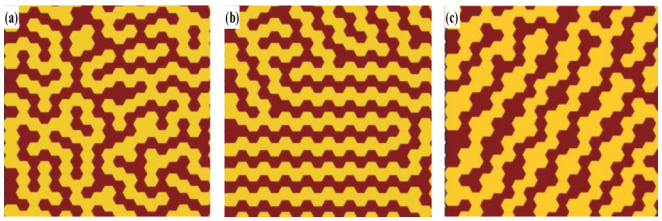

FIG. 4. (Color online) Comparison of MC configurations at $x = 1/2$ obtained with different sets of parameters: (a) $k_BT/J_1 = 0.17$, $J_2/J_1 = 0.21$, and $J_3/J_2 = 0.666$; (b) $k_BT/J_1 = 0.02$, $J_2/J_1 = 0.21$, and $J_3/J_2 = 0.666$; and (c) $k_BT/J_1 = 0.17$, $J_2/J_1 = 0.57$, and $J_3/J_2 = 0.87$ (see text).

From the point of view of electronic properties, the various ordered phases also display very different characteristics. In particular, the presence of the oxide film, with or without Ba adatoms, strongly modifies the Au work function W, with expected consequences on the film reactivity. While the presence of the bare Ti_2O_3 film increases W, further deposition of Ba adatoms lowers it substantially and in a quasilinear way with respect to x. On general grounds, it is well established that the change of work function due to the presence of an oxide ultrathin film on a metal has three contributions which come from the compression of the metal electrons at the interface (negative contribution), the interfacial charge transfer, and the change in the oxide film rumpling [43–45]. In the present case, the large Au electronegativity always results in interfacial electron transfer from the film towards the support, which lower W, while the oxide film rumpling with the oxygen moving outwards increases W.

In the bare Ti_2O_3 film, the rumpling is very large (0.7 Å) due to the strong binding to the gold surface which induces large epitaxial compressive strains. Its associated dipole overcomes the charge transfer and electron compression dipoles, which results in a positive ΔW. A similar situation was discussed in relation to the Moiré pattern produced by MgO islands on Au(111) [46].

At variance, in the $Ba_xTi_2O_3$ films ($x \neq 0$), increasingly large electron transfer to the support takes place as more and more Ba is deposited. Via the electrostatic coupling mechanism by which the electrostatic field exerted by this interfacial dipole distorts the film in such a way as to produce an opposing dipole [47,48], the film rumpling increases, but not enough to counterbalance the large negative contribution to ΔW of the charge transfer.

V. CONCLUSION

Ternary oxide $Ba_xTi_2O_3$ ultrathin films with variable Ba coverage x were created on Au(111) substrates and studied using an approach involving both experiment and theory. STM was able to provide experimental evidence of the film structure, and first principles calculations and MC simulations accurately

modeled the results. Depending on x several ordered phases were identified as well as a disordered labyrinthlike phase. The structural evolution as a function of x is rationalized using a lattice gas model with first-, second-, and third-nearest-neighbor Ba-Ba repulsive interactions $J_{1,2,3}$. MC simulations using $J_{1,2,3}$ values produced by the first principles calculations show an excellent agreement with STM images at all coverages ($0 \leqslant x \leqslant 2/3$).

The physics underlying the structural characteristics of these films is driven by the charge transfer which occurs between the electropositive Ba atoms and the highly electronegative support. This gives rise to interfacial dipole moments which result in effective dipole-dipole Ba-Ba interactions, whose range is a key factor in understanding the Ba ordering. The dipoles also induce an increasingly large film rumpling with increasing x, through an electrostatic coupling mechanism. An efficient reduction of the gold work function with increasing x results. This will significantly affect the film reactivity. Our results suggest that, due to their structural and electronic flexibility, these ultrathin films are promising materials for various types of applications related to adsorption and reactivity, or as patterned supports for the growth of size-selected clusters.

ACKNOWLEDGMENTS

We acknowledge support from the COST Action CM1104 *Reducible oxide chemistry, structure and functions*, from the CNRS-Oxford collaboration scheme, from the John Fell OUP research fund, and from the EPSRC.

[1] W. Mönsch, *Semiconductor Surfaces and Interfaces*, Chapter 14, Springer Series in Surface Science Vol. 26 (Springer-Verlag, Berlin, 2001), pp. 263–328.
[2] J. P. McTague and A. D. Novaco, Phys. Rev. B **19**, 5299 (1979).
[3] O. E. Vilches, Ann. Rev. Phys. Chem. **31**, 463 (1980).
[4] J. Villain and M. B. Gordon, Surf. Sci. **125**, 1 (1983).
[5] O. M. Magnussen, Chem. Rev. **102**, 679 (2002).
[6] D. E. Hooks, T. Fritz, and M. D. Ward, Adv. Mat. **13**, 227 (2001).
[7] W. Weiss and W. Ranke, Prog. Surf. Sci. **70**, 1 (2002).
[8] H.-J. Freund and G. Pacchioni, Chem. Soc. Rev. **37**, 2224 (2008).
[9] N. Nilius, Surf. Sci. Rep. **64**, 595 (2009).
[10] Q.-H. Wua, A. Fortunelli, and G. Granozzi, Int. Rev. Phys. Chem. **28**, 517 (2009).
[11] F. P. Netzer, F. Allegretti, and S. Surnev, J. Vac. Sci. Technol., B **28**, 1 (2010).
[12] C. Wu, M. S. J. Marshall, and M. R. Castell, J. Phys. Chem. C **115**, 8643 (2011).
[13] N. Nilius, E. D. L. Rienks, H.-P. Rust, and H.-J. Freund, Phys. Rev. Lett. **95**, 066101 (2005).
[14] S. Benedetti, F. Stavale, S. Valeri, C. Noguera, H.-J. Freund, J. Goniakowski, and N. Nilius, Adv. Func. Mater. **23**, 75 (2013).
[15] F. Silly and M. R. Castell, J. Phys. Chem. B **109**, 12316 (2005).
[16] C. Becker, A. Rosenhahn, A. Wiltner, K. von Bergmann, J. Schneider, P. Pervan, M. Milun, M. Kralj, and K. Wandelt, New J. Phys. **4**, 75 (2002).
[17] M. Schmid, G. Kresse, A. Buchsbaum, E. Napetschnig, S. Gritschneder, M. Reichling, and P. Varga, Phys. Rev. Lett. **99**, 196104 (2007).
[18] J. Repp, G. Meyer, F. E. Olsson, and M. Persson, Science **305**, 493 (2004).
[19] M. Sterrer, T. Risse, U. M. Pozzoni, L. Giordano, M. Heyde, H. P. Rust, G. Pacchioni, and H.-J. Freund, Phys. Rev. Lett. **98**, 096107 (2007).
[20] J. Goniakowski, C. Noguera, L. Giordano, and G. Pacchioni, Phys. Rev. B **80**, 125403 (2009).
[21] R. Ouyang and W. X. Li, Phys. Rev. B **84**, 165403 (2011).
[22] L. Giordano, G. Pacchioni, C. Noguera, and J. Goniakowski, Top. Catal. **56**, 1074 (2013).
[23] Z. Novotny, G. Argentero, Z. M. Wang, M. Schmid, U. Diebold, and G. S. Parkinson, Phys. Rev. Lett. **108**, 216103 (2012).
[24] Z. Novotny, N. Mulakaluri, Z. Edes, M. Schmid, R. Pentcheva, U. Diebold, and G. S. Parkinson, Phys. Rev. B **87**, 195410 (2013).
[25] G. S. Parkinson, Z. Novotny, G. Argentero, M. Schmid, J. Pavelec, R. Kosak, P. Blaha, and U. Diebold, Nat. Mater. **12**, 724 (2013).
[26] G. Barcaro, A. Fortunelli, and G. Granozzi, Phys. Chem. Chem. Phys. **10**, 1876 (2008).
[27] X. F. Yang, A. Wang, B. Qiao, J. Li, J. Liu, and T. Zhang, Acc. Chem. Res. **46**, 1740 (2013).
[28] C. Wu and M. R. Castell, Surf. Sci. **606**, 181 (2012).
[29] E. Almahmoud, I. Kornev, and L. Bellaiche, Phys. Rev. B **81**, 064105 (2010).
[30] S. Förster, M. Huth, K-M. Schindler, and W. Widdra, J. Chem. Phys. **135**, 104701 (2011).
[31] H. L. Meyerheim, A. Ernst, K. Mohseni, I. V. Maznichenko, J. Henk, S. Ostanin, N. Jedrecy, F. Klimenta, J. Zegenhagen, C. Schlueter, I. Mertig, and J. Kirschner, Phys. Rev. Lett. **111**, 105501 (2013).
[32] R. Gaynutdinov, M. Minnekaev, S. Mitko, A. Tolstikhina, A. Zenkevich, S. Ducharme, and V. Fridkin, Physica B **424**, 8 (2013).
[33] S. Förster, K. Meinel, R. Hammer, M. Trautmann, and W. Widdra, Nature (London) **502**, 215 (2013).
[34] C. Wu, K. Kruska, and M. R. Castell, Surf. Sci. **618**, 94 (2013).
[35] J. P. Perdew and Y. Wang, Phys. Rev. B **45**, 13244 (1992).
[36] P. E. Blöchl, Phys. Rev. B **50**, 17953 (1994); G. Kresse and D. Joubert, *ibid.* **59**, 1758 (1999).
[37] G. Kresse and J. Hafner, Phys. Rev. B **47**, 558 (1993); G. Kresse and J. Furthmüller, *ibid.* **54**, 11169 (1996).
[38] R. F. W. Bader, Chem. Rev. **91**, 983 (1991).
[39] G. Henkelman, A. Arnaldsson, and H. Jonsson, Comput. Mater. Sci. **36**, 354 (2006); W. Tang, E. Sanville, and G. Henkelman, J. Phys.: Condens. Matter **21**, 084204 (2009).
[40] G. Barcaro, S. Agnoli, F. Sedona, G. A. Rizzi, A. Fortunelli, and G. Granozzi, J. Phys. Chem. C **113**, 5721 (2009).
[41] J. R. Iglesias, S. Gonçalves, O. A. Nagel, and M. Kiwi, Phys. Rev. B **65**, 064447 (2002).

[42] J. Escrig, D. Altbir, M. Jaafar, D. Navas, A. Asenjo, and M. Vazquez, Phys. Rev. B **75**, 184429 (2007).
[43] L. Giordano, F. Cinquini, and G. Pacchioni, Phys. Rev. B **73**, 045414 (2006).
[44] L. Giordano, G. Pacchioni, J. Goniakowski, N. Nilius, E. D. L. Rienks, and H.-J. Freund, Phys. Rev. B **76**, 075416 (2007).
[45] J. Goniakowski and C. Noguera, Interface Sci. **12**, 93 (2004).
[46] N. Nilius, S. Benedetti, Y. Pan, P. Myrach, C. Noguera, L. Giordano, and J. Goniakowski, Phys. Rev. B **86**, 205410 (2012).
[47] J. Goniakowski and C. Noguera, Phys. Rev. B **79**, 155433 (2009).
[48] J. Goniakowski, L. Giordano, and C. Noguera, Phys. Rev. B **81**, 205404 (2010).